Inhomogeneous Aging in Lithium-Ion Batteries Caused by Temperature Effects

Sabine Paarmann,* Kathrin Schuld, and Thomas Wetzel*

Lithium-ion batteries (LIBs) are widely used as electrochemical energy storage devices due to their advantages in energy and power density as well as their reliability. One research focus is the cyclic lifetime of LIB, where the influence of thermal conditions during cycling is not yet completely understood. In previous publications, investigations on the cyclic aging behavior of LIB under various thermal boundary conditions are presented, including defined temperature gradients and temperature transients. Thereupon, herein, the results of cell openings and an extensive postmortem study with analyses of scanning electron micrographs, electrode thickness, X-ray diffraction, and inductively coupled plasma optical emission spectroscopy are presented, evaluated, and correlated with the thermal conditions. The results reveal significant variations on the electrode and atomic scale for the different thermal boundary conditions during cycling. The electrodes exposed to a temperature gradient exhibit an inhomogeneous distribution of aging behavior that directly correlates with the local temperature. Cycling with superimposed transient temperatures reveals fundamentally different aging effects. With this knowledge, critical temperature conditions can be avoided in applications to prolong cyclic lifetime.

1. Introduction

Lithium-ion batteries (LIBs) are utilized in numerous applications ranging from mobile phones to electric vehicles as electrochemical energy storage devices. A major advantage of LIB compared to other storage technologies is their high energy and power density. Still, the energy density, cost, safety, and battery lifetime have optimization potential.[1,2]

Lifetime is of concern for the acceptance in society and ecological sustainability, particularly of electric vehicles, as well as the use in second-life applications. It is known that cyclic aging is impacted by the stress factors C-rate,[3–12] depth of discharge,[6–8,11,13,14] state of charge (SoC) range,[5] and temperature.[3,5–10,15–24] However, there is still a lack of understanding the mechanisms of degradation and their interplay, which leaves room for improvement.[25]

The batteries' degradation, performance, and usable energy depend on the internal temperature. Therefore, common recommendations are to operate LIB within the temperature range of about 15–35 °C, and a maximum temperature of about 55 °C should not be exceeded.[26,27] An optimum temperature of around 25 °C is often assumed, whereas warmer and colder temperatures lead to accelerated degradation.

External cooling can actively counteract the internal heat generation caused by both irreversible dissipation and reversible entropic effects. However, this temperature control induces temperature gradients inside the cell[28] and, depending on the temperature control strategy, also temporal temperature changes. For high C-rates, and thus a larger internal heat generation, temperature differences in the cell of more than 10 K may arise.[29]

The open-circuit potential and the internal cell resistance are temperature-dependent. Thus, nonuniformities in temperature cause an inhomogeneous current distribution and lead to nonuniform SoC within the cell.[30] As mentioned, degradation mechanisms like chemical or structural changes depend on various stress factors and often interact. Their effects can be observed in almost all cell components.[5,31–34] Mostly, the focus is on SEI growth, lithium plating, or particle cracking as the main drivers of aging.[20,35,36] Thus, the postmortem analysis of this work will focus on those three mechanisms. We will show how inhomogeneous temperature conditions influence the (non-)uniformity of the observed aging, identify the primary cause of degradation, and discuss how critical temperature inhomogeneities are. Additionally, we show that fundamentally different aging mechanisms occur when the temperature changes with time during cycling.

1.1. Solid Electrolyte Interface

Current, temperature, and voltage impact solid electrolyte interface (SEI) growth.[37,38] Temperature determines the reaction kinetics of SEI formation.[39] At elevated temperatures, the SEI layer grows faster, becoming more porous and unstable.[40] In LiPF$_6$ systems, the SEI is thermally unstable at temperatures above 60 °C[40,41] and reacts with the electrolyte or active

S. Paarmann, K. Schuld, T. Wetzel
Institute of Thermal Process Engineering (TVT)
Karlsruhe Institute of Technology (KIT)
76137 Karlsruhe, Germany
E-mail: sabine.paarmann@kit.edu; thomas.wetzel@kit.edu

The ORCID identification number(s) for the author(s) of this article can be found under https://doi.org/10.1002/ente.202200384.

material.[42] Increasing the temperature even further, unstable components convert to more durable species like Li_2CO_3.[43,44] The deposition of constantly new reaction products on the surface may cause clogging of pores.[45,46] SEI evolution and its characteristics can also be affected by transition metal dissolution, an aging effect at the cathode.

Additionally, the volume expansion during (de-)lithiation of the graphite causes mechanical stress, leading to fracture. The SEI is the weakest material and, therefore, more prone to rupture than graphite.[47] The particle fracture creates fresh graphite surface that reacts again with the electrolyte to new SEI, causing more loss of active lithium. Verma et al.[42] provide a broad overview of other parameters influencing SEI. The sensitivity of SEI growth on the aforementioned conditions leads to inhomogeneous SEI properties if those conditions are inhomogeneously distributed.[48]

1.2. Lithium Deposition

Plating describes the phenomenon during charging when lithium ions are reduced and deposited as metal on the anode surface instead of intercalating into the graphite lattice structure. Literature broadly agrees that this lithium deposition originates from limitations either in the charge transfer or the lithium diffusion in the graphite. Typically charging with high currents or at cold temperatures,[48] especially when combined with an already high SoC,[7] are associated with plating.[23,40,49] Li et al.[50] provide an overview of lithium deposition and its main aspects, like when it occurs, its morphology, how it is influenced, and how it potentially interacts with the SEI. Lithium deposition is a spatially inhomogeneous process that gets more uniform with higher temperatures.[51,52] Generally, lithium deposits preferably at the edges of the electrode sheet as the lithium concentration increases faster there.[53] This so-called edge effect even occurs when the anode is oversized. Although, according to conventional theories, mainly low temperatures lead to plating, it may also be observed at moderate temperatures.[20] In addition, Carter et al.[54] report plating for charging during a temperature transient. They also showed that plating is not limited to high currents if interelectrode temperature gradients are present.[55,56] Then even conditions of 35 °C as average temperature and a current of C/5 can lead to increased depositions. Those findings indicate that plating is less well understood than it might appear. For inhomogeneous temperatures parallel to the electrode, plating is observed in the warmer cell regions as the higher current dominates.[53] Thereby, the location but not the severity of plating[57] is influenced.

The lithium loss due to deposition is partly reversible and is restored after the so-called stripping process.[58] The irreversibly plated lithium, however, reacts with electrolyte to SEI, becomes electrically isolated, and therefore "dead lithium."[51,53]

1.3. Mechanical Stress at the Cathode

A critical aging mechanism of the cathode active material is mechanical degradation leading to disturbed electronic pathways within the composite cathodes and, therefore, to higher contact resistance.[59] Primarily at high voltages, cracks emerge at the

boundaries of the primary particles.[60] This intergranular cracking can mainly be attributed to the strong anisotropic changes of the crystal structure during lithium (de-)intercalation.[61] Therefore, the SoC range during cycling has a higher impact than the temperature. Still, during cycling between the cutoff voltages with a constant current, the temperature impacts the SoC range as the overpotentials depend on temperature. Thus, at higher temperatures higher/lower SoC are reached before the cutoff voltages are hit. Additionally, the exposure of fresh surface to the electrolyte accelerates structural damage and mechanical disintegration.[60]

Furthermore, mechanical degradation on the atomic level is relevant as lattice parameters might change during long-term cycling. **Figure 1** shows the crystal structure of LCO as an example for layered oxides with a hexagonal unit cell and the lattice parameters a and c. Irreversible changes in the crystal structure from rhombohedral to electrochemically inactive cubic mainly occur at the particle surface, reducing the specific capacity of the active material[62] and increasing the charge transfer resistance. This process is accelerated at high cathode potentials.[1,60,61] Especially at fresh surfaces originating from particle cracking, transition metals dissolve.[63] This affects the SEI, where the transition metals alter its formation and lead to an increased loss of lithium. Manganese is prone to metal dissolution, but also nickel, cobalt, and rarely aluminum can be found in the SEI.

Overall, the aging mechanisms at the cathode are less sensitive to temperature than those on the anode, yet the SoC (range) is decisive for its degradation.

Observing the aging mechanisms, it is noticeable that they highly depend on temperature and are hardly homogeneous and at most statistically distributed. The SEI is heterogeneous in terms of its components, and it comprises crystalline and amorphous parts.[65] Plating occurs preferentially at the edges and is extremely localized and inhomogeneous.[48,51] In addition, the morphology changes depend on the conditions, which means there is not the one kind of lithium deposition.[66,67] Plating is
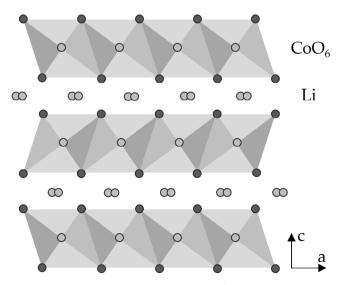

Figure 1. Crystal structure of LCO as example for layered oxides with a hexagonal unit cell and the lattice parameters c and a.

also influenced by uneven temperature and strongly enhanced when the thermal gradient is perpendicular to the electrode layers.[56] Nonuniform SEI and plating, covering the surface, decrease the electrode area, which in turn increases the inhomogeneity of impedance and current density in the cell.[68] So, it is reasonable to infer that a nonuniform temperature distribution leads to inhomogeneous aging effects in the cell. Evidence of how inhomogeneous temperature distributions affect the aging mechanisms during cycling is scarce. Thus, this question is addressed in this publication. The knowledge of a maximum temperature difference that a cell can tolerate without significantly accelerated degradation is most useful for any application.

The results presented here are one aspect in a doctoral thesis[30] and are closely related to our previous cyclic aging study on the impact of temperature boundary conditions on the overall aging quantified by means of capacity fade and resistance increase. The calendar aging of this cell type is considered elsewhere.[69]

In this work, the electrodes of the cycled cells are investigated separately in a postmortem analysis considering electrode, particle, and atomic level. To reveal potential inhomogeneities, methods are chosen that can resolve the properties locally and samples are taken from different locations of the electrodes. After an optical inspection, scanning electron microscopy (SEM) is used, the electrode thickness measured, and X-ray diffraction (XRD) and inductively coupled plasma optical emission spectroscopy (ICP-OES) are performed to evaluate the aging effects that took place. Combining these complementary methods provides a comprehensive understanding of the mechanisms that occur during cell aging. Thus, a conclusion can be drawn as to which of the aforementioned main drivers of aging contribute to which extent to cell aging and how this differs for different thermal boundary conditions. This postmortem analysis will identify how different thermal conditions impact the aging effects and identify the most critical condition.

2. Temperature-Dependent Cell Aging

The commercial pouch cells SLPB 8043140H5 from Kokam Co., Ltd. with a capacity of 3 Ah were cycled under different thermal boundary conditions, including temperature gradients and transients. A detailed explanation of the experimental test setup, the results, the evaluation, and interpretation of the results on the overall aging behavior are given in our previous publications.[70,71] Here, we briefly outline the boundary conditions and summarize the results necessary.

The cells were cycled with a constant current of 3 C (9 A) over the whole SoC range (2.7–4.2 V) at the three temperature levels 0, 25, and 50 °C. Those temperatures, homogeneously distributed over the cell, are typical aging conditions when the temperature influence is considered over a relevant range of application. They are referred to as homogeneous stationary (HS) conditions and serve as the reference cases and basis for comparison for the inhomogeneous and transient thermal boundary conditions. A temperature gradient over the length of the cell specifies the second group of thermal conditions (inhomogeneous stationary [IS]). This gradient spans between two of the temperature levels, respectively, resulting in a magnitude of either 25 or 50° K temperature difference. In the transient cases (homogeneous transient [HT]), the temperature switches during (dis-)charge

between two of the temperatures levels, so the cells are exposed to regular temperature changes over time.

The change in capacity and internal resistance per equivalent full cycle (EFC), based on the standard capacity at beginning of life (BoL) and 25 °C, was evaluated to quantify the aging progress as a function of temperature. This aging rate is shown, as an example, for the capacity in **Figure 2**. The capacity fade $\Delta C_{C/20}$ per EFC is plotted as a function of the temporal and spatial average temperature. Each marker represents the results of one thermal boundary condition. The green squares show the capacity fade of the HS cases, the gray diamonds the IS cases, while the salmon circles represent the HT ones. These marker shapes and colors represent the different groups of conditions throughout the article. The results in the graph show that an aging function (black line) composed of two exponential functions describes the capacity fade for all stationary conditions (HS, IS). The cells cycled under a temperature gradient age according to their average temperature. In contrast, the cells with a transient temperature (HT) exhibit a different aging behavior that does not correlate with the average temperature.

The temperature level, in particular, is decisive for the aging rate even with an inhomogeneous temperature distribution. However, cells that are cycled under a temperature gradient over the length of the cell exhibit an overall aging behavior that corresponds closely to the average temperature. That is even valid for the extreme magnitude of a 50 K difference. Cycling with superimposed temperature changes leads to fundamentally different aging rates. To understand these different behavior, we need to open the cells and perform a postmortem analysis. Therefore, the cells are opened under an inert gas atmosphere, and the electrodes are examined with different methods to get a profound understanding of the aging effects. At cell opening the cells had reached EFCs between 5000 and 9000, except for the cells at HS temperature of 0 °C, which only reached around 900 EFC. For the exact number of EFC of each cell, the reader is referred to the Supporting Information.
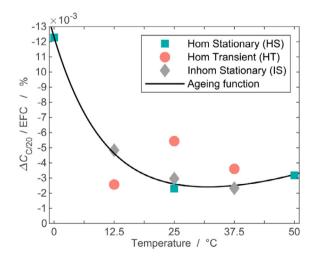

Figure 2. Aging rate as capacity fade per EFC depending on the spatial and temporal average temperature for the thermal boundary conditions. Reproduced with permission under the terms of the Creative Commons CC BY license.[71] Copyright 2020, the Authors. Published by MDPI.

3. Results and Discussion

This section presents the results of the postmortem analysis. Thereby, the changes relative to the state at BoL are compared for the different boundary conditions. First, the optical alterations at the electrodes are presented, which are noticeable by the naked eye when the cell is opened. Subsequently, the SEM images are shown, and electrode thickness and area-specific weight are analyzed in a mechanical characterization. Then, for selected boundary conditions, the XRD results are presented regarding the change in the lattice structure of the cathode, as well as the concentration of lithium, cobalt, nickel, aluminum, and phosphorus in the anode measured via ICP-OES.

3.1. Visual Inspection

During opening the cells, remarkable changes in comparison to BoL were directly visible. For all aged cells, the severest changes occur in the outer layers, which are shown in **Figure 3**.

3.1.1. Homogeneous Stationary

Compared to BoL, the cell cycled at HS 25 °C (HS25 °C) shows a slightly grayish deposit at the outermost anode layer and a slightly increased discoloration at the separator edges. The two rows of dots in Figure 3b are visible on each separator layer in each cell and presumably originate from the production
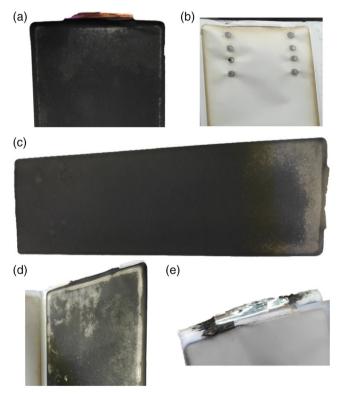

Figure 3. Photographs during cell openings. a) Anode of HS0 °C with some plating, b) discolored separator of HS50 °C, c) anode of IS0/50 °C with plating in the coldest quarter, d) massive plating on the HT0/50 °C anode, and e) dead lithium (black) close to the cathode tab of HT0/50 °C.

process. The most remarkable difference of HS0 °C is an irregular blotchy anode surface, with a clear indication of lithium plating close to the anode current collector and the edges where the anode overlaps the cathode (Figure 3a). This edge effect is a typical phenomenon for lithium plating.[53] Compared to HS0 °C, there occured only minor changes at the condition HS50 °C. The most noticeable change is the strong brownish discolouration of the separator (Figure 3b).

3.1.2. Inhomogeneous Stationary

For the cell exposed to a temperature gradient between 0 and 50 °C, Figure 3c shows the distinct plating visible on the anode localized at the coldest quarter close to the anode tab. The silvery/gray cover layer is discernable throughout the cell stack. Furthermore, the separator has a grayish coloration comparable to the HS50 °C cell. This might be related to very small deposits and particle fragments from the electrodes.[73,74] IS0/25 °C also exhibits clear plating from the anode tab where 0 °C was applied during cycling up to the electrode's center toward the cathode tab. This large area of partially thick planar plating on the surface potentially lengthens the diffusion paths[75] and thus could explain the comparatively large increase in polarization resistance that was observed in the cyclic aging study.[71] The edge effect is evident, but otherwise, the lithium deposition is randomly distributed on the surface. Compared to the IS0/50 °C, the cell with IS0/25 °C shows much less plating and significantly more compared to HS0 °C. Probably, this can be related to lower overpotentials at higher average temperatures. Cycling between the cutoff voltages then leads to higher SoC for a higher average temperature and at high SoC plating is more likely. The cell with a gradient between 25 and 50 °C does not reveal any striking differences compared to HS25 °C. Assuming a linear temperature profile, the significant lithium plating is limited to the coldest cell area where temperatures between 0 and about 12 °C are present. This finding indicates that temperature effects dominate over increased current density at regions with higher temperatures. However, this is in contradiction with the results from Campbell et al.,[53] who found increased plating in the warm region due to the higher current density there.

3.1.3. Homogeneous Transient

The cells charged and discharged with a transient temperature exhibit signs of massive loss of lithium. First, lithium plating on the surface occurs when a temperature level of 0 °C is involved. The anode surface of HT0/25 °C is covered homogeneously with small areas of metallic deposits, while HT0/50 °C shows inhomogeneous patches (Figure 3d). Second, a significant quantity of black friable and soft extra material appears in the cells that were temporarily exposed to 50 °C (HT0/50 °C and HT25/50 °C). It is found at the anode side of the separator, not on, but adhered to the electrode and mainly close to the cathode tab. It even grows from between the separator layers out of the cell stack, which is observable after removing the pouch foil and shown in Figure 3e. In minimal amounts, this also appears in the other cells, either in the separator fold or near the cathode tab. A flame test for material detection via the characteristic

**ADVANCED
SCIENCE NEWS**

www.advancedsciencenews.com

Energy Technology

Generation, Conversion, Storage, Distribution

www.entechnol.de

emission spectrum shows a red flame coloration, indicating lithium with the two main spectral lines at 671 nm.[76] Presumably, the material is dead lithium that deposited rather than intercalated and then reacted with electrolyte to SEI. The localized material close to the cathode tab might be due to nonuniform electrolyte filling.[77] It could also be related to the significantly lower pressure at the edge of the cell stack than between the electrodes. Therefore, mossy lithium can deposit and grow further there. Li et al.[50] provide similar considerations, claiming that lithium is deposited in a mossy morphology when the SEI is elastic. As a large amount of dead lithium arises only for HT0/50 °C and HT25/50 °C, temperature changes seem critical for this phenomenon – when high temperature is involved. Probably, the temperature increase during charging from 0 to 50 °C reduces the overpotentials and changes the balance of the rate-determining processes so that lithium plating occurs. Similar observations are reported by Carter et al.[54] for charging at transient temperatures. This can explain the accelerated aging rate for HT thermal conditions noticed for capacity fade in our previous study.[71]

3.2. SEM

SEM images of the aged electrodes in **Figure 4** show detailed changes for the different thermal conditions. Primary particles of NCA increasingly lose their adhesion to each other at elevated temperature resulting in reduced integrity and finally cracking of secondary particles along the boundaries between the primary particles. This is visible in the cross sections of the cathode for the HS50 °C boundary condition in the first row of Figure 4, indicated by yellow circles. After cycling at 50 °C, the primary particles of each secondary particle are well identifiable, and some are completely broken. This is also evident in the close up of the surface circled in yellow. At 25 °C, only some secondary particles break during cycling, while at 0 °C, the primary particles composing the secondary particles are not discernible, just as in the BoL state.

The particle rupture at higher temperature probably is a consequence of higher mechanical stress caused by phase transformation. At elevated temperatures, the cutoff voltages are reached after a larger charge throughput, and the phase transformation, which occurs mainly at high voltages,[78] is completely undergone. In contrast, the LCO particles do not show signs of particle cracking in the electrode sections analyzed. In addition to the particle cracking of NCA, there are more deposits visible on the cathode surface images for increasing cycling temperature. The cathode that was cycled at 50 °C shows darker patches which seem to be flake-like particles (orange arrows).

The graphite anode does not exhibit any alteration in the cross section, so the images are not shown. However, the inspection of the surface reveals significant modifications. The anode cycled at 0 °C is, in some places, coated with a thick homogeneous layer that looks like it is shrunk on the surface (blue arrows) and is assumed to be one type of morphology of plated lithium. Otherwise, there is little change in the typical flake structure of graphite in this case. For 25 °C, there are minor changes compared to BoL (cp., Supporting Information) as the surface layer, probably SEI, blurs the edges of the flakes slightly more.

The anode cycled at 50 °C exhibits much more nonuniform surface phenomena. Again, the blurring of the edges is visible together with tiny granular deposits in the first picture attributed to electrolyte degradation and SEI. In contrast, clusters of needle-like crystals appear in other regions and the second picture. Presumably, this constitutes another morphology of lithium plating. These findings suggest that the morphology of plated lithium depends on the cycling temperature. While the deposits tend to be needle-like or granular at high temperatures, they are more planar and homogeneous at low temperatures. This observation is supported by Park et al.,[64] who report less dendritic growth for lower temperature and Li et al., who state that for extensive deposition, the morphology is planar.[50]

The electrodes in the cells cycled with a temperature gradient exhibit similar phenomena as described for HS, depending on the local temperature. The only difference for IS0/50 °C is needle-like lithium plating in the cold part of the anode that was not observed in the HS0 °C condition.

The SEM images of the cathode of HT0/50 °C look similar to the cathode HS50 °C with broken NCA particles but slightly more deposits on the surface. The anode partly shows the familiar needle-like structures. Yet, in other parts, a thick surface layer covers the graphite particles. The pressure in the cell probably causes the large amount of plating to compact and form this layer between the anode surface and the separator.

3.3. Mechanical Characterization

In this section we evaluate the changes of thickness and weight of the anode due to aging. **Figure 5** shows the change in anode thickness relative to its initial state at BoL as a function of the local temperature. The cathode layer, on the other hand, does not show a discernible influence of the temperature on the thickness and exhibits only a minor thickness increase or even decrease, so it is not shown here, but in the Supporting Information.

The standard deviation is <0.18% throughout the measurements. Thus, the error bars are smaller than the marker size and therefore not visible in the diagram. In general, the anode thickness increases with higher temperatures. Especially for the HS conditions (green squares), the trend of increasing anode thickness with temperature is evident and almost linear. Waldmann et al.[58] obtained similar cycling results at homogeneous temperature, although they found an S-shaped correlation of anode thickness and temperature instead of an almost linear one.

For the cells with inhomogeneous temperature control (IS), the electrode thickness was measured at both the cold and the warm edges. The thickness at the warm side is indicated in Figure 5 with the light gray diamonds, while the cold side thickness is represented by dark gray diamonds. These thicknesses follow the linear temperature dependency almost perfectly. The slightly higher thickness increase at the cold edge of IS0/25 °C might be due to the high amount of thick lithium plating on the surface. Thus, it can be concluded that the anode thickness is mainly determined by the actual local temperature, independent of other conditions elsewhere.

The thickness changes of the anodes with HT temperature control (HT, salmon circles) stand out, as they are not in line

**ADVANCED
SCIENCE NEWS**

www.advancedsciencenews.com

Energy Technology
Generation, Conversion, Storage, Distribution
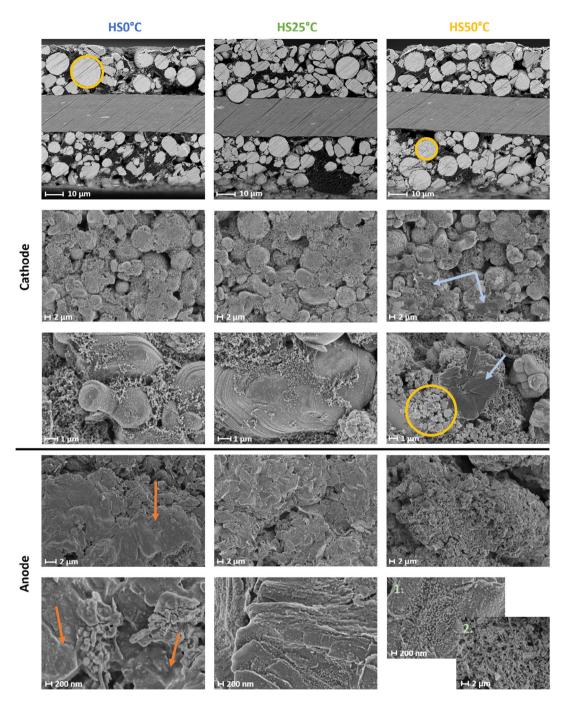
www.entechnol.de

Figure 4. SEM images at EoL of cathode cross section (first row) and surface (second and third row) and the anode surface (fourth and fifth row) for cycling at HS temperature control at 0 °C (first column), 25 °C (second column), and 50 °C (third column).

with the other data. Here, the temperature value is the temporal average. The anodes of HT0/50 °C (circle at 25 °C) and HT25/50 °C (circle at 37.5 °C) are slightly thicker, as their average temperature would suggest, while those of HT0/25 °C (circle at 12.5 °C) are thinner. These findings are similar to the capacity fade during cycling, which is more significant for the first two and less for the last one than expected according to the aging function[71] (cp., Figure 2).

The relative increase in anode weight in **Figure 6** resembles the picture of the layer thickness, although the relative differences are much lower. The standard deviation is still <0.18%, but due to the scaling of the y-axis, the error bars are now discernable in the plot. There is a higher increase in weight at higher temperatures for the cells cycled at HS conditions. In contrast to the layer thickness, the weight at the edges with applied temperature gradients does not correspond to that after cycling at respective
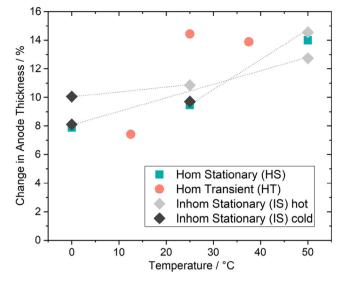
**ADVANCED
SCIENCE NEWS**
www.advancedsciencenews.com

Energy Technology
Generation, Conversion, Storage, Distribution
www.entechnol.de

Figure 5. Increase in the anode thickness relative to BoL depending on the local temperature for the different thermal boundary conditions during cycling.
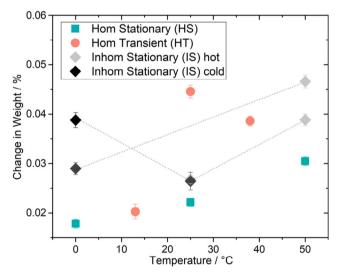

Figure 6. Increase in the anode weight relative to BoL depending on the local temperature for the different thermal boundary conditions during cycling.

homogeneous temperatures but is higher, both at cold and warm temperatures.

Considering the HT conditions, the weight increase for HT0/25 °C is relatively low, while it is much higher for HT25/50 °C and especially HT0/50 °C. It therefore follows the trend observed so far.

The results suggest that the effects contributing to the increase in thickness and weight are purely temperature-dependent and do not depend on current. Side reactions and thus SEI growth are accelerated at high temperatures and partly contribute to the increase in anode thickness. As the SEI formation is uneven across the depth of the graphite anode and most intense close

to the separator,[45] it should be detectable with surface-sensitive characterization techniques. However, there is no covering layer visible in the SEM micrographs that would indicate an increase of the anode thickness of almost 15%. Thus, we calculated the lithium loss the SEI growth would have incorporated as a rough estimate. The estimation and the assumptions are summarized in the Supporting Information. The results for the hot part of the IS25/50 °C cell are presented in the following, as the anode thickness is highest in this case.

Assuming the SEI consists of pure dilithium ethylene dicarbonate (Li$_2$EDC; C$_4$H$_4$Li$_2$O$_6$), with a molar volume of $\tilde{V}_{SEI} = 9.6 \cdot 10^{-5} \frac{m^3}{mol}$ and an overall porosity ε of 10%, Equation (1) can be employed to calculate the number of moles lost in the SEI.

$$\tilde{M}_{Li} = \frac{2}{\tilde{V}_{SEI}} \cdot (1 - \varepsilon) \cdot A_{Anode} \cdot \Delta s \qquad (1)$$

With the surface area of all anode sheets $A_{Anode} = 0.292 \, m^2$ and a thickness increase of $\Delta s = 6.2 \, \mu m$, the amount of lithium lost in the SEI would be 0.046 mol. Another way to calculate the amount of lithium in the SEI is based on X-ray photoelectron spectroscopy (XPS) measurements, which is very surface sensitive and resolves only the first few nanometers of the surface, so the composition of the SEI is revealed. It gives a lithium concentration of 23.5 at% at the anode surface. Using this value, an overall amount of lithium in the SEI of 0.034 mol can be calculated. Although the two values differ, they are in the same order of magnitude. If the anode thickness increase is completely attributed to the SEI growth, even the lowest increase of $\Delta s = 3.1 \, \mu m$ for HT0/25 °C consumed 0.024 and 0.017 mol lithium, respectively. A similar calculation can be done regarding the increase in electrode weight. It has to be noted that the cells with the highest/lowest increase in layer thickness are not the same that reveal the highest/lowest increase in weight. Assuming it is solely due to the SEI, between 0.011 mol (HS0 °C) and 0.028 mol (IS0/50 °C hot), is lost, depending on the thermal condition.

To illustrate the implication of these numbers, they are compared to the amount of lithium present in the anode. The amount of lithium in the aged anodes obtained from ICP-OES ranges from 0.076 mol (HS0 °C) to 0.113 mol (IS0/50 °C).

Figure 7 shows the correlation of the change Δ in thickness and weight increase to the amount of lithium in the aged anodes. As the ICP-OES was only performed for selected samples, the number of markers is reduced. The results for the HS conditions are shown as green squares, and the color of the inner square indicates the respective temperature. Additionally, the data for HT0/50 °C and IS0/50 °C are included. Two aggregations of data points can be identified for both thickness and weight gain. One at low lithium amounts and low weight/thickness increase. Those markers belong to low-to-medium temperature conditions, while the second cluster at higher moles of lithium is associated with higher temperatures or a temperature transient.

Furthermore, there is a linear trend for the weight while there is none for the thickness increase. Although these calculations are rough estimates, they imply that the weight increase is mainly due to lithium deposition or SEI growth, while another effect contributes to the thickness increase.
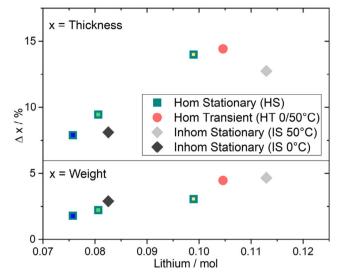
Figure 7. Thickness and weight increase correlated with the amount of lithium determined with ICP-OES for different thermal boundary conditions.

Figure 8. Change in lattice parameters a and c relative to BoL for NCA.

Assumably, cycling leads to increased solvent cointercalation and exfoliation so that the graphite particles expand over time, contributing to the thickness increase. Furthermore, the SEI consists not only of Li_2EDC but various other decomposition products containing fluor and phosphorus. Transition metals at the anode and originating from the cathode probably do not significantly affect the weight, as their concentration is low (cp., ICP-OES). Still, they impact the SEI growth and composition, so they might indirectly affect the substantial thickness and weight increase during cycling. This might explain the relatively large thickness increase compared to the lower weight increase.

3.4. XRD

XRD is used to investigate potential distortions of the crystal structure of the cathode active material by determining the lattice parameters. XRD reveals that for all thermal boundary conditions, lattice parameter a decreases while lattice parameter c increases for both NCA and LCO. The only exception is parameter a of LCO at HT0/25 °C, which increases slightly. These alterations are more pronounced in NCA. The results for NCA are shown in **Figure 8**, while the diagram for LCO can be found in the Supporting Information. The expansion along the x-axis indicates less lithium within the structure.[79]

At first glance, there is little temperature dependency in the parameter variation in Figure 8. Still, for lattice parameter c, the values for cells with HS temperature control increase with rising temperature. Temperature gradients have different effects for the warm and cold regions. In the warm region, the change in the lattice parameters is about the same as for homogeneous temperature control, while in the cold area, there are greater differences than with the equivalent homogeneous temperature control.

Moreover, the homogeneously transient cycled cells once again exhibit a pattern that deviates from their average
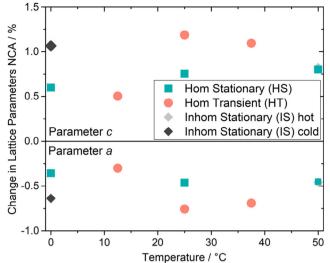
temperature comparable to that of the layer thickness increase. Accordingly, HT0/50 °C and HT25/50 °C have a more significant change in c, while it is relatively small for HT0/25 °C. The measurements for lattice parameter a do not indicate a considerable temperature dependency, but the HT cells show a larger decrease in the lattice parameter. The increase in c combined with the decrease in a leads to a distortion of the crystal structure where the layers are more widely spaced while the atoms within a layer converge. Besides the change in lattice parameters, a slight shift of the peaks in one or the other direction can be observed in the spectrum. However, this cannot be correlated with the boundary conditions and is therefore not presented here. No splitting of one or more peaks can be observed as, for example, Maher et al. did.[80] Therefore, it can be assumed that a hexagonal crystal structure is still present after cycling, in which only the c/a ratio has increased, leading to a decreased lithium stoichiometry, which is supported by the literature.[14,18] In terms of crystal structure, NCA appears to be more prone to these effects than LCO.

3.5. ICP-OES

The concentration of aluminum, cobalt, nickel, lithium, and phosphorus in the anodes is measured by ICP-OES and shown in **Figure 9**. As the measurement is very costly, there is fewer data available. The trend of increasing lithium concentration at higher temperatures is evident in Figure 9a. It increases for HS temperature control with rising temperature, and for applied gradients (IS0/50 °C) and especially for temperature changes (HT0/50 °C), it is even further increased.

Similar results are obtained for phosphorus shown in Figure 9b. The highest phosphorus concentration is found in the HT0/50 °C cell. However, there seems to be no temperature influence below 25 °C, while the concentration increases significantly at 50 °C. The measured values are in the same order of magnitude but slightly higher as found in the literature.[16,63] This can be explained by the long duration of the experiment
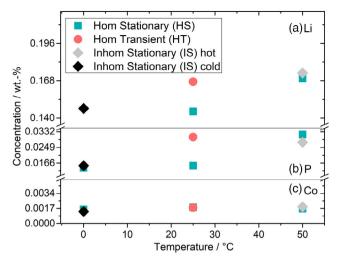
**ADVANCED
SCIENCE NEWS**
www.advancedsciencenews.com

Energy Technology
Generation, Conversion, Storage, Distribution
www.entechnol.de

Figure 9. Concentration in weight percentage of a) lithium, b) phosphorous, and c) cobalt in the cycled anode active material.

and the high number of EFC reached in this work. The weight percentage of lithium is significantly lower here but depends strongly on the voltage at cell opening and is therefore difficult to compare.

Transition metals are present in all samples. Figure 9c shows the cobalt concentration as an example. Thus, their dissolution has occurred at the cathode during cycling. The largest amount is found for cobalt, followed by nickel and aluminum, which corresponds to the order of their stability. There is no significant trend with respect to the temperature. The cobalt concentration increases slightly with rising temperature up to 0.19 wt% for the anode at 50 °C in the cell cycled with a temperature gradient. Aluminum has a higher concentration only at 50 °C, especially for the anode for HS50 °C, while there is a slight decrease for nickel.

The results for phosphorous and lithium correlate positively with the temperature dependency of the anode thickness, suggesting that the thickness increase is at least partly due to SEI growth after all. This SEI growth is likely accelerated by higher temperatures leading to higher reactions rates and cobalt incorporating into the SEI and altering it. The relative impact of temperature increase and the presence of transition metals on SEI growth cannot be distinguished. Still, as increased temperature causes enhanced cross-talk, it is the relevant factor. However, there must be another relationship that explains the behavior of cells under HT temperature control. Both the film thickness and XRD indicate increased aging with temperature changes at medium- and high-temperature levels, which is also confirmed in the weight fractions of phosphorus and lithium from ICP-OES. Nevertheless, no increased fraction of transition metals appears in the anode for these boundary conditions. The change of the lattice parameters in the crystal structure is not directly related to their dissolution.

The coefficients of thermal expansion vary strongly between the materials and might cause accelerated aging when the cell is subject to temporal temperature changes. The thermal expansion coefficient ranges from 55 to 66 µm K^{-1} for graphite,

depending on the degree of intercalation.[81] For NCA and LCO, there is no literature data, but for the whole cell, values range from 1.1 µm K^{-1} (LCO/C)[82] to 5.49 µm K^{-1} (NMC/C).[83] These values are large enough to induce mechanical stress inside the cell, which is known to affect degradation during cycling.[84] Still, this seems unlikely as aging is accelerated at moderate and high temperatures, but is milder at HT0/25 °C, although the expansion coefficients are constant over the entire temperature range. Whether the thermal expansion actually contributes to the observed aging behavior or not cannot conclusively be clarified here.

3.6. Correlation of Results

The cell cycled at a homogeneous temperature of 0 °C shows less change than expected, considering that this temperature is commonly supposed to promote lithium plating. Yet, the cell in this investigation shows only minor signs of lithium deposition in the visual inspection, SEM, and the lithium concentration in the anode is relatively low. The cells at a low-temperature level seem to benefit from the constant current (CC) cycling without constant voltage (CV) phase because the high SoC, which is critical for plating, is avoided by reaching the voltage limits early. Thus, temperature and voltage effects cannot be separated completely. Also, the particle fracture and reduced cohesion of the NCA secondary particles in cells cycled at 50 °C can be attributed to the higher SoC reached due to the higher temperature.

An evident temperature dependency can be shown for the anode thickness, increasing with temperature. This may partly be attributed to enhanced SEI growth at higher temperatures which is supported by the increased lithium and phosphorus concentration at the anode found by ICP-OES. Still, this cannot explain all of it. Lithium deposition at cold temperatures seems to have a minor impact on the thickness increase.

However, the SEM images of the surface do not show an increased concentration of decomposition products forming a severe surface layer. Whether a great proportion of the SEI is developed in the bulk of the electrode cannot be proven as the porosity changes cannot be reliably determined. Either way, according to our estimation, the measured thickness increase does not correlate with the amount of lithium in the anode. Thus, it is presumably not only due to SEI growth. Presumably, higher temperatures lead to solvent cointercalation and exfoliation, resulting in these high anode thicknesses.

The weight increase for the HS conditions exhibits a temperature dependency that is less pronounced than that of the thickness increase. In contrast to the thickness increase, it correlates linearly with the lithium amount in the anode. Thus, it could be associated with lithium deposition and SEI growth.

The ICP-OES measurements reveal that there are transition metals present at the anode which is due to their dissolution at the cathode. Although they are known to enhance SEI growth, their concentration does not correlate with the lithium and phosphorus concentration. Furthermore, for the HS conditions, the results do not suggest a strong temperature dependency.

In contrast, the crystal lattice becomes slightly more distorted at elevated temperatures, which is probably due to lower lithium concentrations and indicates a loss of capacity. Additional signs

ADVANCED
SCIENCE NEWS

www.advancedsciencenews.com

Energy Technology
Generation, Conversion, Storage, Distribution

www.entechnol.de

of mechanical degradation appear in the SEM cross sections, indicating a reduced cohesion of the NCA secondary particles up to particle fracture. NCA is clearly more affected by the mentioned changes than LCO.

The influence of temperature gradients on the anode is already apparent at the cell opening. Lithium plating is visible as silverish deposition on the anode surface in the cold part up to about 12 °C, assuming a linear temperature gradient. The differences between warm cell regions and cold ones are also apparent in the specific electrode weight and layer thickness. While the layer thickness of the anode with homogeneous temperature control matches that at the corresponding temperature with the gradient applied, the specific weight for the anode cycled under a temperature gradient is generally increased. This supports that they are not induced by the same mechanisms. Nevertheless, both lithium concentration and lattice parameters show the same results for high temperatures whether a temperature gradient was applied or not. For cold temperatures, the variation is slightly stronger for the cell cycled with a gradient.

In this study, the inhomogeneity is provoked by extreme gradients with temperature differences of 25 and 50 K over the length of the cell. Assumably, the statistical distribution of all the mechanisms would diminish the measurable effect if the temperature differences were considerably smaller. However, none of the cells has reached the knee point, from which aging accelerates dramatically. This effect is also known as sudden death and can be triggered by different mechanisms and/or their combinations.[85] Therefore, it cannot be excluded that this transition point is reached earlier in the cells with gradient and inhomogeneous aging effects despite similar aging with and without temperature gradients. So even with the temperature-dependent alterations during aging revealed by the postmortem analysis, a maximum temperature difference over the length of the cell cannot be defined.

In contrast to temperature gradients, temporal temperature changes lead to different aging effects. At cell opening, HT0/50 °C shows by far the greatest amount of lithium plating and dead lithium, followed by HT25/50 °C. In ICP-OES, the amount of lithium and phosphorus is also significantly increased for both cells, and the layer thickness of the anode increases excessively for those two conditions. The lattice parameters of the cathode also change the most for these two cells. This would mean that the crystal lattice distortion is not the driver for the transition metal dissolution.

While increased aging occurs for temperature changes over the entire temperature range or at a high-temperature level, it is consistently milder for HT0/25 °C than the average temperature would indicate. The most significant aging mechanism at cold temperatures is said to be plating. However, this is not limited to these conditions but also occurs at high temperatures.

The coefficient of thermal expansion as a possible cause seems unlikely as aging is accelerated at moderate and high temperatures, but is milder at HT0/25 °C, although the expansion coefficients are constant over the entire temperature range.

As the boundary condition is applied at the surface, the temperature will change there first before the cell core adjusts to the new temperature. Therefore, a through-plane temperature gradient exists. This directionality of the interelectrode gradient may be a dominant effect that causes the different aging behavior observed in this study.

The reason for the mild aging of HT0/25 °C might be the combination of a small SoC range at 0 °C and the stripping of reversibly plated lithium at the higher temperature of 25 °C. Probably, at 25 °C, the stripping process is more favorable compared to the SEI growth on the plated lithium. In contrast, SEI growth is faster and more dominant at 50 °C.

4. Conclusion

The postmortem analysis reveals variations on the electrode and atomic scale for the different thermal boundary conditions during cycling that complement and sometimes contrast the common understanding.

The temperature dependency of the various aging mechanisms is still valid when there is an applied temperature gradient over the length of the cell. With inhomogeneous temperature distribution, they occur accordingly inhomogeneously and induce an inhomogeneous aging behavior in the cell. This means that the aging effects occur according to the local temperature whether there is a homogeneously distributed temperature in the cell or an in-plane temperature gradient. However, this is limited to the electrode level and does not affect the cells' overall capacity fade and impedance increase which changes according to the average cell temperature, as shown previously.[71]

The presented results prove that temporal temperature changes during cycling provoke an utterly different aging behavior. This is consistently shown by the methods of postmortem analysis (excluding the concentration of transition metals) and has likewise been observed for capacity fade and impedance increase.[71] Here, not only the temperature level but also the magnitude of temperature difference seems important as the aging is most severe for the cell experiences changes between 0 and 50 °C. We assume that the directionality of the interelectrode gradient contributes significantly to this behavior which is in accordance with the findings of Carter et al.[55]

Overall, it can be stated that the most relevant aging mechanisms are the loss of lithium at the anode and the loss of adhesion between secondary particles at the cathode. Harlow et al.[36] suggest monocrystals as cathode active material to prevent particle cracking and state that a rapid formation of a stable SEI is a requirement for a long lifetime of the battery cell as it impedes loss of active lithium. The result presented in this publication support this hypothesis.

5. Experimental Section

The cells under investigation are high-power pouch cells with a counter-tab configuration from Kokam Co., Ltd. (SLPB 8043140H5), with a nominal capacity of 3.2 Ah, a nominal voltage of 3.7 V. The typical experimentally measured discharge capacity at standard conditions (25 °C and C/2) is 3 Ah. Energy dispersive X-ray spectroscopy (EDX) results show the chemistry to be graphite at the anode and an LCO/NCA blend at the cathode. The separator is made of PE, verified by a melting point analysis with differential scanning calorimetry (DSC). XPS reveals that for the electrolyte $LiPF_6$ as conductive salt is used, probably in ethylene carbonate and/or dimethyl carbonate (DMC) as solvent.

Cyclic Aging: A detailed description of the test setup and testing procedure is available in ref. [70]. Self-designed temperature control plates

**ADVANCED
SCIENCE NEWS**

www.advancedsciencenews.com

Energy Technology
Generation, Conversion, Storage, Distribution

www.entechnol.de

were employed to control the temperature directly at the cell surface. They comprised liquid cooling and heating channels. They were supplied by thermostats, which guaranteed high-temperature stability independent of the thermal load. This allowed the temperature boundary conditions to be precisely applied onto the electrode stack and the cell tabs. The plates also ensured the mechanical clamping of the cells. Springs provided a defined and uniform surface pressure of $p = 3.3 \, \text{N cm}^{-2}$ applied to the electrode stack of each cell.

The cycling was performed with the cell test device XCTS from BaSyTec, while the periodical check-up measurements were carried out with the CTS Lab from BaSyTec due to the higher voltage and current accuracy.

Postmortem Analysis: To ensure the comparability of the results, all cells have been discharged before opening with a C-rate of C/20, then C/40, followed by a CV phase at 2.83 V, which corresponds to the relaxation voltage at BoL after complete discharge to 0% SoC. This procedure was suggested by Kobayashi et al.[62] and reduces the influence of overpotentials due to different impedance rises during aging. It is difficult to ensure the same state of intercalation for all the cells. This procedure comes close but still assumes that no major shift of the electrode balancing occurs due to different cycling conditions. The cells are not completely discharged to 0 V but remain in their regular operating window to avoid material changes unrelated to aging.[31] Comparing the capacity before cell opening with that from the last check-up ensures that no further changes have occurred over time. Then, the cells were opened in a glove box under an inert gas atmosphere of argon with ceramic tools to avoid short circuits. Necessary equipment into which water can diffuse was dehumidified at 60 °C for at least eight hours before use. Anode and cathode sheets were separately washed in DMC for about 2 min to remove residual conducting salt, following the recommendations from Waldmann et al.[31] Then the electrodes were dried, and the samples were prepared according to the requirements of the subsequent analyses. To identify the effect of inhomogeneous temperature control, samples as close as possible to the warm and cold edge were taken for the IS cells.

Electrode Weight and Thickness: To determine the area-specific weight of the electrodes, five electrode coins with a diameter of 20 mm were stamped out with a punch. They had a defined area so that their weight can be compared. They were ejected from the glove box, weighed on a precision scale, and the average value was calculated. Subsequently, the thickness of the double-coated electrode was carefully measured on those coins with a digital indicator from Mitutoyo.[72] The results of this mechanical gauge were verified for BoL with a thickness evaluation of the cross sections from SEM images.

SEM: SEM images of anode and cathode were taken from the active material surface and a cross section of the current collector with coated active material on both sides. Approximately 5 × 5 mm sections have been cut out of the electrode using ceramic scissors. Still in the glove box, the samples were sealed with Parafilm in glass vials with rolled rim and snapcap. Then they were transported to the microscopes, and the vials were only opened shortly before the sample was transferred into the device. Thus, the time of air exposure is kept as short as possible. Own observations prove that brief contact with air is not critical for imaging, which is consistent with the literature[86,87] even for samples with substantial lithium plating. The surface was analyzed with a secondary electron (SE) detector and an accelerating voltage of 2 kV with magnifications between 10 000 and 60 000.

The cross sections were polished with an ion beam milling system from Leica Microsystems[88] to achieve a planar surface. Therefore, argon ions are accelerated with a voltage of 6 kV and remove the outermost surface mechanically. In the hard tabs and cathode particles, grooves from this treatment are visible in some locations. The cross-sectional images were taken with a magnification of 1000–3000 with a backscattered diffraction (BSD) detector and an accelerating voltage of 5 kV.

Mercury Porosimetry: To measure the porosity, the washed electrodes were cut into pieces of 5 × 7 mm with ceramic scissors to fit into the test tube. The mercury porosimetry was carried out with Pascal 140 and Pascal 440 devices from the manufacturer POTEC to achieve a pressure range from 0.01 kPa to 400 MPa. This pressure range corresponds approximately to pore radii from 58 μm to 1.8 nm.

Table 1. Porosity and layer thickness of the investigated cell at BoL.

	Anode	Cathode	Separator
Porosity [%]	26	29	38
Layer thickness [μm] active material (current collector)	36 (13)	27 (19)	13

The porosity $\varepsilon_{\text{meas}}$ measured by the device refers to the entire sample. It, therefore, includes the current collector on which the active material is coated. To calculate the porosity ε_{AM} of the active material coating, its impact has to be eliminated using the ratio of the layer thicknesses, according to the equation below.

$$\varepsilon_{\text{AM}} = \varepsilon_{\text{meas}} \cdot \left(1 + \frac{s_{\text{CC}}}{s_{\text{ges}} - s_{\text{CC}}}\right) \tag{2}$$

The analyzed range of pore sizes is limited to between 0.01 and 4 μm following Froboese et al.[89] Pore sizes with smaller diameters are negligible and larger pores result solely from the spaces between the cut electrodes. The values for the porosity and layer thickness are given in **Table 1**.

XRD: XRD spectra were obtained from the powder of the cathode active material. It was carefully scraped off from the current collector with a scalpel. The obtained powder was filled under argon atmosphere in glass vials with rolled rim and snap-cap sealed with Parafilm. The samples were transferred to the D8 Advance diffractometer by Bruker.[90] The X-rays with a wavelength of 1.51484 Å originated from a copper source. The Bragg–Brentano arrangement of the diffractometer covers angles from 10° to 90° divided into 7820 steps, with an acquisition time of 3 s each. After the measurement, the background noise was subtracted, and the $K_{\alpha 2}$ separation was conducted. This data consisting of angle and intensity was evaluated, and the lattice parameters a and c are calculated in MATLAB. This calculation was verified with XRD measurements at different SoC as literature data are available for comparison.[91,92]

ICP-OES: ICP-OES was measured on electrode coins with 20 mm in diameter and a weight of 75–77 mg. Two coins were used from each cell, and duplicate determinations were performed on two cell samples. Before the actual measurement, acid digestion has to be conducted to bring the components of the sample into solution. Graphite was only partially digested, but all other elements were dissolved using a microwave system from MLS Application. In addition to the samples, two acid blanks were also measured to avoid allocating any impurities to the samples. The acid digestion was carried out with 6 mL HNO_3 (65%), 1 mL H_2O_2 (30%), and 1 mL deionized water. An immediate reaction with the samples takes place. Therefore, it was necessary to wait briefly before sealing the containers and placing them in the microwave system. This operated a three-step program for graphite digestion with temperatures between 220 and 260 °C and powers of 700–1000 W, with the pressure rising to about 30 bar. This procedure takes 36 min and is shown in the Supporting Information.

Finally, the samples needed to cool down. A dark, bluish supernatant (liquid) with a black residue of graphite remained. Subsequently, they were decanted into volumetric flasks and diluted to 25 mL with deionized water (MilliQ).

The actual measurement was carried out with the iCAP 7000 from ThermoFisher Scientific.[93] The solution was dosed and mixed with argon to form an aerosol, which was excited in the measuring chamber with a plasma at up to 900 °C.

Supporting Information

Supporting Information is available from the Wiley Online Library or from the author.

[1] B. Scrosati, J. Garche, W. Tillmetz, *Advances in Battery Technologies for Electric Vehicles*, Woodhead Publishing, Oxford 2015, https://doi.org/10.1016/B978-1-78242-377-5.00010-8.

[2] M. Li, J. Lu, Z. Chen, K. Amine, *Adv. Mater.* 2018, 30, 1800561.

[3] Y. Wu, P. Keil, S. F. Schuster, A. Jossen, *J. Electrochem. Soc.* 2017, 164, A1438.

[4] J. Li, E. Murphy, J. Winnick, P. A. Kohl, *J. Power Sources* 2001, 102, 294.

[5] K. Kleiner, P. Jakes, S. Scharner, V. Liebau, H. Ehrenberg, *J. Power Sources* 2016, 317, 25.

[6] Y. Preger, H. M. Barkholtz, A. Fresquez, D. L. Campbell, B. W. Juba, J. Romàn-Kustas, S. R. Ferreira, B. Chalamala, *J. Electrochem. Soc.* 2020, 167, 120532.

[7] M. Ecker, P. S. Sabet, D. U. Sauer, *Appl. Energy* 2017, 206, 934.

[8] S. F. Schuster, T. Bach, E. Fleder, J. Müller, M. Brand, G. Sextl, A. Jossen, *J. Energy Storage* 2015, 1, 44.

[9] W. Liu, C. Delacourt, C. Forgez, S. Pelissier, in *2011 IEEE Vehicle Power and Propulsion Conf.*, IEEE, Piscataway, NJ September 2011, pp. 1–6, https://doi.org/10.1109/VPPC.2011.6043110.

[10] M. S. D. Darma, M. Lang, K. Kleiner, L. Mereacre, V. Liebau, F. Fauth, T. Bergfeldt, H. Ehrenberg, *J. Power Sources* 2016, 327, 714.

[11] M. Lewerenz, D. U. Sauer, *J. Energy Storage* 2018, 18, 421.

[12] G. Ning, B. Haran, B. N. Popov, *J. Power Sources* 2003, 117, 160.

[13] M. Ecker, N. Nieto, S. Käbitz, J. Schmalstieg, H. Blanke, A. Warnecke, D. U. Sauer, *J. Power Sources* 2014, 248, 839.

[14] S. Watanabe, M. Kinoshita, T. Hosokawa, K. Morigaki, K. Nakura, *J. Power Sources* 2014, 258, 210.

[15] D. Aurbach, B. Markovsky, A. Rodkin, M. Cojocaru, E. Levi, H. J. Kim, *Electrochim. Acta* 2002, 47, 1899.

[16] T. Waldmann, M. Wilka, M. Kasper, M. Fleischhammer, M. Wohlfahrt-Mehrens, *J. Power Sources* 2014, 262, 129.

[17] R. B. Wright, C. G. Motloch, J. R. Belt, J. P. Christophersen, C. D. Ho, R. A. Richardson, I. Bloom, S. A. Jones, V. S. Battaglia, G. L. Henriksen, T. Unkelhaeuser, *J. Power Sources* 2002, 110, 445.

[18] P. Ramadass, B. Haran, R. White, B. N. Popov, *J. Power Sources* 2002, 112, 614.

[19] M. Schimpe, M. E. von Kuepach, M. Naumann, H. C. Hesse, K. Smith, A. Jossen, *J. Electrochem. Soc.* 2018, 165, A181.

[20] K. Jalkanen, J. Karppinen, L. Skogström, T. Laurila, M. Nisula, K. Vuorilehto, *Appl. Energy* 2015, 154, 160.

[21] I. Bloom, S. A. Jones, V. S. Battaglia, G. L. Henriksen, J. P. Christophersen, R. B. Wright, C. D. Ho, J. R. Belt, C. G. Motloch, *J. Power Sources* 2003, 124, 538.

[22] F. Leng, C. M. Tan, M. Pecht, *Sci. Rep.* 2015, 5, 1.

[23] T. Waldmann, B. I. Hogg, M. Kasper, S. Grolleau, C. G. Couceiro, K. Trad, B. P. Matadi, M. Wohlfahrt-Mehrens, *J. Electrochem. Soc.* 2016, 163, A1232.

[24] A. Friesen, X. Mönnighoff, M. Börner, J. Haetge, F. M. Schappacher, M. Winter, *J. Power Sources* 2017, 342, 88.

[25] G. J. Offer, T. S. O´Connor, M. De Marco, *Opportunities for Disruptive Advances Through Engineering for Next Generation Energy Storage*, Zenodo 2020, https://doi.org/10.5281/zenodo.3931338.

[26] G. Xia, L. Cao, G. Bi, *J. Power Sources* 2017, 367, 90.

[27] A. Pesaran, S. Santhanagopalan, G.-H. Kim, *Addressing the Impact of Temperature Extremes on Large Format Li-Ion Batteries for Vehicle Applications*, 30th International Battery Seminar, Ft. Lauderdale, FL, USA 2013.

[28] M. Fleckenstein, O. Bohlen, B. Bäker, *World Electr. Veh. J.* 2012, 5, 322.

[29] T. Waldmann, G. Bisle, B.-I. Hogg, S. Stumpp, M. A. Danzer, M. Kasper, P. Axmann, M. Wohlfahrt-Mehrens, *J. Electrochem. Soc.* 2015, 162, A921.

[30] S. Paarmann, *How Non-Uniform Temperatures Influence the Performance and Aging of Lithium-Ion Batteries*, Karlsruhe Institute of Technology, Karlsruhe 2021. [Online], https://doi.org/10.5445/IR/1000139983.

[31] T. Waldmann, A. Iturrondobeitia, M. Kasper, N. Ghanbari, F. Aguesse, E. Bekaert, L. Daniel, S. Genies, I. J. Gordon, M. W. Löble, E. De Vito, *J. Electrochem. Soc.* 2016, 163, A2149.

[32] C. Schlasza, P. Ostertag, D. Chrenko, R. Kriesten, D. Bouquain, in *2014 IEEE Transportation Electrification Conf. and Expo (ITEC)*, IEEE, Piscataway, NJ 2014, https://doi.org/10.1109/ITEC.2014.6861811.

[33] J. P. Fath, D. Dragicevic, L. Bittel, A. Nuhic, J. Sieg, S. Hahn, L. Alsheimer, B. Spier, T. Wetzel, *J. Energy Storage* 2019, 25, 100813.

[34] J. S. Edge, S. O' Kane, R. Prosser, N. D. Kirkaldy, A. N. Patel, A. Hales, A. Ghosh, W. Ai, J. Chen, J. Yang, S. Li, *Phys. Chem. Chem. Phys.* 2021, 23, 8200.

[35] J. Vetter, P. Novák, M. R. Wagner, C. Veit, K. C. Möller, J. O. Besenhard, M. Winter, M. Wohlfahrt-Mehrens, C. Vogler, A. Hammouche, *J. Power Sources* 2005, 147, 269.

[36] J. E. Harlow, X. Ma, J. Li, E. Logan, Y. Liu, N. Zhang, L. Ma, S. L. Glazier, M. M. Cormier, M. Genovese, S. Buteau, *J. Electrochem. Soc.* 2019, 166, A3031.

[37] F. German, A. Hintennach, A. LaCroix, D. Thiemig, S. Oswald, F. Scheiba, M. J. Hoffmann, H. Ehrenberg, *J. Power Sources* 2014, 264, 100.

[38] I. V. Veryovkin, C. E. Tripa, A. V. Zinovev, S. V. Baryshev, Y. Li, D. P. Abraham, *Nucl. Instrum. Methods Phys. Res., Sect. B* 2014, 332, 368.

[39] S. S. Zhang, K. Xu, T. R. Jow, *Electrochim. Acta* 2004, 49, 1057.

[40] A. Tomaszewska, Z. Chu, X. Feng, S. O'kane, X. Liu, J. Chen, C. Ji, E. Endler, R. Li, L. Liu, Y. Li, *eTransportation* 2019, 1, 100011.

[41] H. H. Lee, C. C. Wan, Y. Y. Wang, *J. Electrochem. Soc.* 2004, 151, A542.

**ADVANCED
SCIENCE NEWS**

www.advancedsciencenews.com

Energy Technology
Generation, Conversion, Storage, Distribution

www.entechnol.de

[42] P. Verma, P. Maire, P. Novák, *Electrochim. Acta* **2010**, *55*, 6332.

[43] J. T. Li, J. Swiatowska, A. Seyeux, L. Huang, V. Maurice, S.-G. Sun, P. Marcus, *J. Power Sources* **2010**, *195*, 8251.

[44] M. N. Richard, J. R. Dahn, *J. Electrochem. Soc.* **1999**, *146*, 11.

[45] M. Klett, P. Svens, C. Tengstedt, A. Seyeux, J. Światowska, G. Lindbergh, R. Wreland Lindström, *J. Phys. Chem. C* **2015**, *119*, 90.

[46] D. P. Abraham, J. L. Knuth, D. W. Dees, I. Bloom, J. P. Christophersen, *J. Power Sources* **2007**, *170*, 465.

[47] I. Laresgoiti, S. Käbitz, M. Ecker, D. U. Sauer, *J. Power Sources* **2015**, *300*, 112.

[48] N. Ghanbari, T. Waldmann, M. Kasper, P. Axmann, M. Wohlfahrt-Mehrens, *J. Phys. Chem.* **2016**, *120*, 22225.

[49] M. Petzl, M. A. Danzer, *J. Power Sources* **2014**, *254*, 80.

[50] Z. Li, J. Huang, B. Yann Liaw, V. Metzler, J. Zhang, *J. Power Sources* **2014**, *254*, 168.

[51] R. W. Atkinson, R. Carter, C. T. Love, *Energy Storage Mater.* **2019**, *22*, 18.

[52] A. Mistry, C. Fear, R. Carter, C. T. Love, P. P. Mukherjee, *ACS Energy Lett.* **2019**, *4*, 156.

[53] I. D. Campbell, M. Marzook, M. Marinescu, G. J. Offer, *J. Electrochem. Soc.* **2019**, *166*, A725.

[54] R. Carter, E. J. Klein, T. A. Kingston, C. T. Love, *Front. Energy Res.* **2019**, *7*, 144.

[55] R. Carter, Todd A. Kingston, Robert W. Atkinson, Mukul Parmananda, Matthieu Dubarry, Conner Fear, Partha P. Mukherjee, Corey T. Love, *Cell Rep. Phys. Sci.* **2021**, *2*, 100351.

[56] R. Carter, C. T. Love, *ACS Appl. Mater. Interfaces* **2018**, *10*, 26328.

[57] C. Fear, M. Parmananda, V. Kabra, R. Carter, C. T. Love, P. P. Mukherjee, *Energy Storage Mater.* **2021**, *35*, 500.

[58] X.-G. Yang, S. Ge, T. Liu, Y. Leng, C.-Y. Wang, *J. Power Sources* **2018**, *395*, 251.

[59] M. Kerlau, M. Marcinek, V. Srinivasan, R. M. Kostecki, *Electrochim. Acta* **2007**, *52*, 5422.

[60] Y. Ruan, X. Song, Y. Fu, C. Song, V. Battaglia, *J. Power Sources* **2018**, *400*, 539.

[61] C. Xu, K. Märker, J. Lee, A. Mahadevegowda, P. J. Reeves, S. J. Day, M. F. Groh, S. P. Emge, C. Ducati, B. Layla Mehdi, C. C. Tang, *Nat. Mater.* **2021**, *20*, 84.

[62] H. Kobayashi, M. Shikano, S. Koike, H. Sakaebe, K. Tatsumi, *J. Power Sources* **2007**, *174*, 380.

[63] J. A. Gilbert, I. A. Shkrob, D. P. Abraham, *J. Electrochem. Soc.* **2017**, *164*, A389.

[64] R. Hausbrand, G. Cherkashinin, H. Ehrenberg, M. Gröting, K. Albe, C. Hess, W. Jaegermann, *Mater. Sci. Eng. B: Solid State Mater. Adv. Technol.* **2015**, *192*.

[65] Z. Ahmad, V. Venturi, H. Hafiz, V. Viswanathan, *J. Phys. Chem.* **2021**, *125*, 11301.

[66] C. T. Love, O. A. Baturina, K. E. Swider-Lyons, *ECS Electrochem. Lett.* **2014**, *4*, A24.

[67] B. S. Vishnugopi, A. Verma, P. P. Mukherjee, *J. Phys. Chem. C* **2020**, *124*, 16784.

[68] K. Rumpf, A. Rheinfeld, M. Schindler, J. Keil, T. Schua, A. Jossen, *J. Electrochem. Soc.* **2018**, *165*, A2587.

[69] D. Werner, S. Paarmann, T. Wetzel, *Batteries* **2021**, *7*, 28.

[70] D. Werner, S. Paarmann, A. Wiebelt, T. Wetzel, *Batteries* **2020**, *6*, 13.

[71] D. Werner, S. Paarmann, A. Wiebelt, T. Wetzel, *Batteries* **2020**, *6*, 12.

[72] 'Mitutoyo, Produkt: Digitale Messuhr ID-H, CEE Netzteil', °https://shop.mitutoyo.de/web/mitutoyo/de_DE/mitutoyo/01.04.04A/Digital%20Messuhr%20ID-H%2C%2°CEE%20AC-Adapter/$catalogue/mitutoyoData/PR/543-563D/index.xhtml (accessed May 2021).

[73] D. P. Abraham, J. Liu, C. H. Chen, Y. E. Hyung, M. Stoll, N. Elsen, S. MacLaren, R. Twesten, R. Haasch, E. Sammann, I. Petrov, *J. Power Sources* **2003**, *119–121*, 511.

[74] W. Ai, L. Kraft, J. Sturm, A. Jossen, B. Wu, *J. Electrochem. Soc.* **2020**, *167*, 013512.

[75] B. Stiaszny, J. C. Ziegler, E. E. Krauß, J. P. Schmidt, E. Ivers-Tiffée, *J. Power Sources* **2014**, *251*, 439.

[76] C. Mavroukakis-Karagounis, I. Papadopoulou, M. Papadopoulou, C. Makedonas, *Chem. Teach. Int.* **2019**, https://doi.org/10.1515/cti-2018-0013.

[77] A. Mistry, *Re: Plating Issue*, E-Mail communication **2021**.

[78] K.-J. Park, J. Y. Hwang, H. H. Ryu, F. Maglia, S. J. Kim, P. Lamp, C. S. Yoon, Y. K. Sun, *ACS Energy Lett.* **2019**, *4*, 1394.

[79] H. Wang, J. F. Whitacre, *J. Energy Storage* **2021**, *35*, 102244.

[80] K. Maher, R. Yazami, *J. Power Sources* **2014**, *247*, 527.

[81] C. Bindra, V. A. Nalimova, D. E. Sklovsky, W. A. Kamitakahara, J. E. Fischer, *Phys. Rev. B* **1998**, *57*, 5182.

[82] B. Rieger, S. V. Erhard, K. Rumpf, A. Jossen, *J. Electrochem. Soc.* **2016**, *163*, A1566.

[83] Y. Zhao, F. B. Spingler, Y. Patel, G. J. Offer, A. Jossen, *J. Electrochem. Soc.* **2019**, *166*, A27.

[84] J. Cannarella, C. B. Arnold, *J. Power Sources* **2014**, *245*, 745.

[85] P. M. Attia, A. Bills, F. Brosa Planella, P. Dechent, G. dos Reis, M. Dubarry, P. Gasper, R. Gilchrist, S. Greenbank, D. Howey, O. Liu, E. Khoo, Y. Preger, A. Soni, S. Sripad, A. G. Stefanopoulou, V. Sulzer, *arXiv:2201.02891 [cond-mat, physics:physics]* **2022**, [Online], http://arxiv.org/abs/2201.02891 (accessed: February 2022).

[86] M. Lewerenz, A. Warnecke, D. U. Sauer, *J. Power Sources* **2017**, *369*, 122.

[87] N. Williard, B. Sood, M. Osterman, M. Pecht, *J. Mater. Sci.: Mater. Electron.* **2011**, *22*, 1616.

[88] Leica Microsystems GmbH, Routeplanner, https://www.leica-microsystems.com/products/sample-preparation-for-electron-microscopy/p/leica-em-tic-3x/ (accessed: May 2021).

[89] L. Froboese, P. Titscher, B. Westphal, W. Haselrieder, A. Kwade, *Mater. Charact.* **2017**, *133*, 102.

[90] Bruker, *Battery Research : Characterizing The Future*, John Wiley & Sons Ltd, Chichester **2019**.

[91] R.-Z. Yin, Y.-S. Kim, S.-J. Shin, I. Jung, J.-S. Kim, S.-K. Jeong, *J. Electrochem. Soc.* **2012**, *159*, A253.

[92] R. Robert, C. Bünzli, E. J. Berg, P. Novák, *Chem. Mater.* **2015**, *27*, 526.

[93] J. Hannan, *Tech. Note* **2013**, *43153*.